applied sciences

MDPI

Article

Vibration Control of a Base Structure Using a GVTC Damping Plate Based on the Acoustic Black Hole Effect

Wenxi Liu [1], Yi Zhou [1], Junbo Hu [1,*], Lu Tan [1], Maoting Tan [1], Jiamin Di [2], Jingjun Lou [1] and Qingchao Yang [1]

[1] Naval University of Engineering, Wuhan 430033, China; wxliu777@163.com (W.L.); m23385503@nue.edu.cn (Y.Z.); summer03240106@163.com (L.T.); tanmt_lzjtu@163.com (M.T.); 0905061010@nue.edu.cn (J.L.)
[2] Equipment Support Group, Naval Equipment Department, PLA, Beijing 100038, China; 15195815860@163.com
* Correspondence: husky_86083697@163.com

Abstract

This study addresses the challenge of multi-order resonance in base structures within the low-frequency range (10~300 Hz), a common issue in shipbuilding and aerospace applications. Traditional vibration control methods, including those based on the Acoustic Black Hole (ABH) effect, often undermine base structural integrity, offer limited effective bandwidth, or pose practical implementation challenges. To overcome these limitations, this paper proposes a Gradient Variable-Thickness Composite (GVTC) damping plate for passive vibration control, integrating the ABH effect with anti-resonance theory. The key innovation is an engineering-oriented integrated design characterized by external mounting, multi-level stacking, and efficient shell-element modeling rather than a fundamental modification to the ABH principle itself. The composite plate comprises a uniform-thickness region, a gradient-thickness region, and a damping layer, with thickness variation defined by a power-law function. By tuning geometric and material parameters, the plate's natural frequencies are matched to the base panel's resonant peaks. Employing shell elements over solid elements significantly reduces computational cost while maintaining high accuracy (relative error of the first three natural frequencies < 0.6%). Finite element simulations and experimental tests have demonstrated significant vibration suppression: peak reductions of 10 dB, 12.1 dB, 9.7 dB, and 22.9 dB at 94 Hz, 188 Hz, 244 Hz, and 294 Hz, respectively, under simulation conditions, and 7.5 dB, 11.1 dB, 8.5 dB, and 7 dB at 82 Hz, 172 Hz, 234 Hz, and 286 Hz, respectively, in experiments. The additional mass of the damping plate accounts for only 1.53% of the base panel mass. This work provides a practical and efficient solution for low-frequency vibration control and facilitates the engineering application of ABH technology in high-end equipment.

Keywords: ABH effect; gradient variable-thickness plate; composite damping plate; base panel; low-frequency vibration control

Check for updates

Academic Editor: Junhong Park

Received: 5 January 2026
Revised: 3 February 2026
Accepted: 16 February 2026
Published: 25 February 2026

Copyright: © 2026 by the authors. Licensee MDPI, Basel, Switzerland. This article is an open access article distributed under the terms and conditions of the Creative Commons Attribution (CC BY) license.

1. Introduction

In high-end equipment such as ships and aircraft, the base structure serves as a critical interface between the power equipment and the primary structure. Its vibration control performance directly affects operational stability, equipment longevity, and personnel comfort [1–3]. The vibration generated by the operation of power equipment is transmitted to the hull through the base structure. Therefore, mitigating base vibration and its transmission is critical to reducing the overall structural vibration of the vehicle.

With the development of equipment such as underwater vehicles and large ships towards high-speed and lightweight, the periodic excitation generated by the operation of rotating equipment (such as propulsion motors and pump sets) in the power cabin easily induces significant resonance of the base panel in the low-frequency range. This leads to the transmission of vibration energy through the structure, contributing to excessive cabin noise and even structural fatigue damage [4–6]. Therefore, the development of efficient, lightweight vibration control technologies that preserve the base's inherent strength has emerged as one of the core research directions in the current field of equipment vibration reduction.

Conventional approaches for base vibration control include structural stiffness optimization, the use of rubber isolators, and the application of damping patches [7–9]. Among them, while structural stiffness optimization can adjust the resonance frequency, it exhibits limited adaptability for finalized equipment and easily results in an increase in structural weight; rubber vibration isolators are prone to stiffness softening in the low-frequency range (<100 Hz), resulting in a significant decrease in vibration isolation efficiency [10,11]. While traditional damping patches can dissipate part of the vibration energy, they are limited by the material loss factor, so their effect on suppressing resonance peaks is limited. Moreover, they require a large-area application, which hinders meeting the lightweight requirement [12,13].

The limitations of these methods have prompted researchers to explore vibration control technologies based on new physical effects. For example, from the perspective of structural acoustic design, based on the ABH effect [14], the vibration of the controlled (target) structure is reduced by locally setting gradient variable-thickness plates. As an emerging wave energy regulation mechanism, the ABH effect provides a new idea for low-frequency vibration control. Its core principle is to design gradient variations in structural geometric parameters (e.g., thickness) to enable the wave speed of flexural waves propagating in the structure gradually decaying to zero, enabling the efficient accumulation and dissipation of vibration energy [15–17]. Mironov [14] was the first to theoretically prove that when the structural thickness changes in accordance with a power function ($h(x) = \varepsilon x^m$, $m \geq 2$), zero-reflection and full absorption of flexural waves can be achieved, establishing a theoretical basis for the design of ABH structures. Through numerical simulation and experimental verification, Krylov et al. [18,19] found that the absorption efficiency of one-dimensional ABH wedge beams for flexural waves can reach more than 90%, advancing the application of ABH technology in the vibration control of plate and shell structures.

However, an ideal ABH structure requires the tip thickness to approach zero, which is difficult to achieve in actual processing due to process limitations, resulting in 50~70% flexural wave reflection at the structural truncation and markedly compromising the vibration reduction effect [20,21]. To address this issue, scholars have proposed composite damping design schemes: He Pu et al. [22] pasted high-loss-factor damping materials at the ABH truncation, reducing the reflection coefficient to below 20% for full-frequency vibration suppression of box structures; Zhao Yenan et al. [23] combined ABH with energy harvesters to realize vibration absorption and energy recovery integration; Liu Zuncheng et al. [24] developed an ABH floating raft system by embedding ABH units into the support structure, increasing vibration isolation efficiency by 2~3 dB in the 50~200 Hz band and verifying ABH technology's application potential in complex equipment.

In the engineering application of ABH structures, structural form and installation method are key to vibration reduction efficiency. Xia Jiacheng [25] proposed an embedded ABH plate design by integrating the black hole unit into the base panel; though it enhances vibration reduction, it undermines the base's inherent stiffness. Additionally, the embedded

gradient variable-thickness plate (e.g., in base panels and webs) is limited by the strength and size of the target structure, restricting its vibration control to the medium-to-high frequency range and leaving the low-frequency vibration control of underwater vehicles as a pressing unaddressed challenge. Although larger-scale gradient variable-thickness plates with adjusted target-structure connections may expand the control frequency range, relevant public studies are scarce. Furthermore, existing numerical simulations mostly use solid elements for discretization, resulting in a large unit scale and low calculation efficiency, which hinders this technology's engineering application.

To address the above research gaps, this paper proposes a GVTC damping plate based on the ABH effect for passive vibration control of the base panel in underwater vehicle power cabins. The core research framework, following "theory-design-modeling-simulation-experiment", is structured as follows: first, integrating the ABH principle and anti-resonance theory, a composite structure comprising a uniform thickness region, a gradient variable-thickness region, and a damping layer is designed, with its natural frequency tuned to the base's multi-order vibration peaks by adjusting material and geometric parameters; second, shell element modeling is adopted instead of traditional solid elements to minimize computational load while maintaining calculation accuracy (the relative discrepancy of the first three-order natural frequencies is <0.6%); third, lightweight materials are selected to prevent modifying the base's vibration characteristics; finally, finite element analysis and experimental tests under central and offset excitation scenarios are conducted to validate the damping plate's vibration suppression effect in the 10~300 Hz band and its impact on base strength and weight.

The ABH effect, damping layer compensation for truncated structures, and anti-resonance tuning are well-established theories in the field of passive vibration control [14,22,24–26]. Existing studies have verified the feasibility of ABH-based vibration reduction, and in contrast to the studies mentioned above, this work focuses on engineering integration and design optimization. The primary contributions are threefold: (1) an external installation design that preserves the base structure and simplifies implementation; (2) a multi-level stacking strategy to achieve multi-order resonance control; (3) the adoption of shell element modeling, which significantly reduces computational cost while maintaining accuracy, thereby providing an efficient tool for engineering applications. This study provides an engineering-viable integrated technical solution for low-frequency multi-order vibration control of finalized base structures, and it provides a practical reference for the engineering application of ABH technology in high-end equipment such as ships and aerospace vehicles.

2. Materials and Methods

2.1. ABH Principle

The acoustic black hole (ABH) effect enables the gradual attenuation of flexural wave speeds in thin-walled structures through gradient variations in material properties or geometric parameters (e.g., thickness). In an ideal state, as the thickness of the thin-walled structure approaches zero, the flexural wave velocity decays to zero under non-reflective conditions, which provides the core technical support for passive low-frequency vibration control.

Figure 1 clearly illustrates the propagation mechanism of flexural waves in a one-dimensional ABH structure, acting as a concise summary of the ABH effect. A typical one-dimensional ABH structure is a wedge-shaped beam, whose cross-sectional thickness follows a power function decay (Equation (1)), as shown in Figure 2:

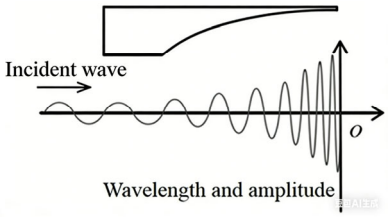
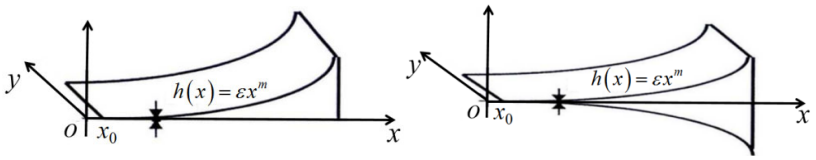


Figure 1. Propagation of flexural waves in one-dimensional ABH structure.



(**a**) Asymmetric ABH wedge edge. (**b**) Symmetric ABH wedge edge.

Figure 2. Wedge edge of a typical one-dimensional ABH structure.

Its thickness expression is shown in Equation (1):

$$h(x) = \varepsilon x^m \tag{1}$$

where $h(x)$ is the thickness of the acoustic black hole structure at position x; ε is a constant; and the power exponent m is a positive rational number, termed the black-hole effect index factor. Mironov has proven that, when the structural thickness variation conforms to this power function curve and the power exponent $m \geq 2$, the basic requirements of an acoustic black hole can be met, achieving zero reflection and full absorption of incident flexural waves [27], which provides a key theoretical basis for structural design.

According to the geometric acoustics analysis method, the control equation for the propagation of flexural waves in a one-dimensional acoustic black hole structure [26,28,29] is shown in Equation (2):

$$\begin{aligned} &\frac{\partial^2}{\partial x^2}\left[D(x)\left(\frac{\partial^2 w}{\partial x^2}+\mu\frac{\partial^2 w}{\partial y^2}\right)\right]+2(1-\mu)\frac{\partial^2}{\partial x\partial y}\left[D(x)\frac{\partial^2 w}{\partial x\partial y}\right] \\ &+\frac{\partial^2}{\partial y^2}\left[D(x)\left(\frac{\partial^2 w}{\partial y^2}+\mu\frac{\partial^2 w}{\partial x^2}\right)\right]-\omega^2\rho h(x)w=0 \end{aligned} \tag{2}$$

Equation (2) represents the biharmonic wave equation governing bending wave propagation in plate structures, derived herein based on the Kirchhoff thin-plate theory. Considering that the thicknesses of the base plate and the GVTC damping plate are much smaller than their in-plane dimensions, the core condition of the Kirchhoff assumption, "thickness much smaller than in-plane dimensions", is fully satisfied. Thus, only bending deformation is considered, and shear deformation is neglected. For one-dimensional ABH wedge structures, the thickness varies only along the x-axis, and wave propagation only involves the gradient in the x-direction. However, the GVTC damping plate investigated herein is a two-dimensional plate structure: the thickness in the gradient-varying region decays exponentially along the x-axis (length direction) while remaining uniform along the y-axis (width direction $(\partial/\partial y) = 0$). Accordingly, the two-dimensional gradient operator $\nabla = (\partial/\partial x)i + (\partial/\partial y)j$ was introduced to extend the one-dimensional wedge theory to the two-dimensional plate configuration, ensuring that Equation (2) accurately characterizes the propagation behavior of bending waves in the target structure.

Where $D(x) = Eh^3(x)/12(1-\mu^2)$ is the bending stiffness of the structure, E is the elastic modulus of the material, μ is the Poisson's ratio of the material; w is the deflection (i.e., the degree of bending deformation of the structure under external forces); ρ is the

density of the material; and $\omega = 2\pi f$ is the circular frequency. By solving Equation (2), the expression for the transverse displacement at any position of the structure can be obtained:

$$w(x) = A(x)e^{i\Phi(x)} \tag{3}$$

where $A(x)$ and $\Phi(x) = k_p\varphi(x,y)$ are the varying displacement amplitude and cumulative phase, respectively. Among them, $k_p = \omega/c_p$ is the wave number of the uniform part of the structure, $c_p = 2c_t\left(1 - c_t^2/c_l^2\right)^{1/2}$ is the phase velocity, and c_t and c_l wave speeds of transverse waves and longitudinal waves in the structure, respectively; $\varphi(x,y) = \varphi'(x) + (\beta/k_p)y$ is the eikonal function, and $\beta = 0$ when the flexural wave is normally incident on the acoustic black hole structure. Substituting Equation (3) into Equation (2), for the equation to hold, both the real part and the imaginary part on the left side of the equation must be zero. Setting the real part to zero and ignoring the high-order derivative terms of $A(x)$ and $\Phi(x)$, the eikonal equation of the flexural wave can be obtained [19,30–33]:

$$\left|\nabla\varphi(x,y)\right|^4 = \frac{k^4(x)}{k_p^4} = n^4(x) \tag{4}$$

$$k(x) = 12^{1/4}k_p^{1/2}(\varepsilon x^m)^{-1/2} \tag{5}$$

where $\nabla = (\partial/\partial x)\boldsymbol{i} + (\partial/\partial y)\boldsymbol{j}$ is the gradient operator; $k(x)$ is the position-dependent wave number, and $n(x)$ is the corresponding refractive index. For the normal incidence of flexural waves ($\beta = 0$), the cumulative phase $\Phi(x)$ can also be expressed as an integral from any position x in the acoustic black hole structure to the wedge edge:

$$\Phi(x) = \int_0^x k(x)dx \tag{6}$$

Combining Equations (5) and (6), it can be seen that, when $m \geq 2$, $\Phi(x)$ tends to infinity, and the wave number of the flexural wave also approaches infinity. This means the wave speed tends to zero, the wave amplitude tends to infinity, and the wave energy will be confined to the edge of the structure, i.e., the "acoustic black hole effect" is generated.

However, due to process limitations in actual manufacturing, the ABH structure cannot achieve a zero tip thickness, and there must be a truncation at the structure edge. Even a very small truncation thickness will significantly degrade the wave control effect of the ABH, markedly increasing the structural reflection coefficient. Calculation results indicate that even an extremely small truncation thickness (e.g., 0.1 mm) can increase the reflection coefficient to 50%~70% [34], drastically reducing the energy accumulation effect. To compensate for this defect, damping materials with high loss factors are pasted in the truncation area. The viscoelastic behavior of the damping layer is characterized in simulations using the complex modulus model $E^* = E(1 + i\eta)$ (where E^* is the complex modulus, E is the elastic modulus, and η is the material loss factor), utilized in simulations to describe the viscoelastic behavior of the damping layer. Through the energy dissipation effect of the damping layer [34–38], the reflection coefficient is effectively reduced. In particular, the tip truncation thickness of the GVTC damping plate in this study is set to 0.2 mm and matched with a high-loss damping material to mitigate truncation-induced reflection losses, thus addressing the contradiction between truncation reflection and vibration reduction performance and providing a key improvement direction for the subsequent design of composite damping plates.

2.2. GVTC Damping Plate

Combining the ABH principle and anti-resonance theory, an external GVTC damping plate (as shown in Figure 3) is designed, which comprises three functional components:

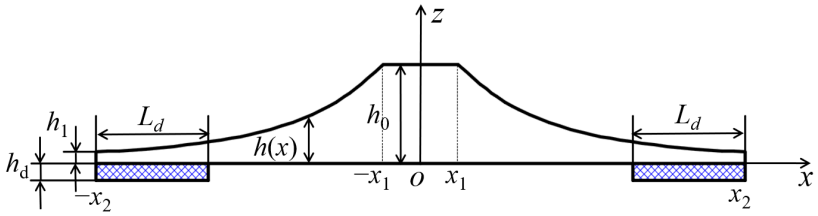


Figure 3. GVTC damping plate.

A uniform thickness region with a thickness of h_0 (length from 0 to x_1, $L = x_2 - x_1$), whose main function is to interface with the controlled base panel through bolts or welding and transmit vibration energy.

A gradient variable-thickness region (length from x_1 to x_2), whose thickness changes gradually according to the power function law to realize the deceleration and accumulation of flexural waves, and its thickness variation expression is:

$$h(x) = \begin{cases} h_0, (0 \le x \le x_1) \\ (h_0 - h_1)\left(\frac{L-x+x_1}{L}\right)^2 + h_1, (x_1 \le x \le x_2) \end{cases} \quad (7)$$

A damping layer with a thickness of h_d (length L_d), covering the outer side of the gradient variable-thickness region. A damping material with a high loss factor is selected to dissipate the accumulated vibration energy and minimize the reflection of flexural waves.

This composite damping plate adopts an external installation design. It eliminates the need for grooves or indentations on the base panel and is only fastened to the panel surface via connectors, thereby preserving the stiffness and strength of the base itself. There is no need to redesign the finalized base structure, significantly enhancing engineering applicability. From the perspective of dynamic characteristics, its core working mechanism is manifested in two key aspects:

ABH effect. After the vibration energy is transmitted from the uniform thickness region to the gradient variable-thickness region, the thickness decays according to the power function, so the wave speed of flexural waves gradually decreases and accumulates at the outer edge. At this time, the damping layer dissipates the accumulated vibration energy as heat via viscoelastic deformation, achieving energy absorption.

Anti-resonance effect. As an additional oscillator, the natural frequency of this composite damping plate can be adjusted by modifying material parameters (such as elastic modulus and density) and geometric parameters (such as the length of the gradient variable-thickness region and minimum thickness). When the natural frequency aligns with the resonance peak frequency of the base panel, the structure generates an anti-resonance phenomenon, which markedly suppresses the vibration response of the base panel at the target frequency.

In addition, compared with the traditional embedded ABH structure, the gradient variable-thickness region of this external composite damping plate is unrestricted by the size of the base structure, and can be designed with a larger scale to broaden the vibration control frequency range. At the same time, its edge lacks structural constraints, offering a larger deformation space, which is more favorable for enhancing the ABH effect and subsequently boosting the vibration reduction efficiency. This provides a technical solution for solving the multi-order resonance problem of the base panel of underwater vehicle equipment in the 10~300 Hz low-frequency range.

3. Vibration Control Research

3.1. Vibration Characteristic Analysis of the Base Panel

To accurately understand the vibration law of the base panel of equipment in the power cabin of underwater vehicles, a complete structural model was established in this study using ABAQUS 2021 finite element analysis software. The model includes two parts: the power cabin and the base of the rotating equipment inside the cabin, as shown in Figure 4. The power cabin is composed of a cabin section, annular ribs, and an end cover. Nine annular ribs are distributed at equal intervals along the outer axial direction of the cabin section, with a spacing of 600 mm between adjacent ribs; the base structure consists of a base panel, reinforcing ribs, and supporting I-beams. The specific geometric parameters of each component are listed in Table 1.

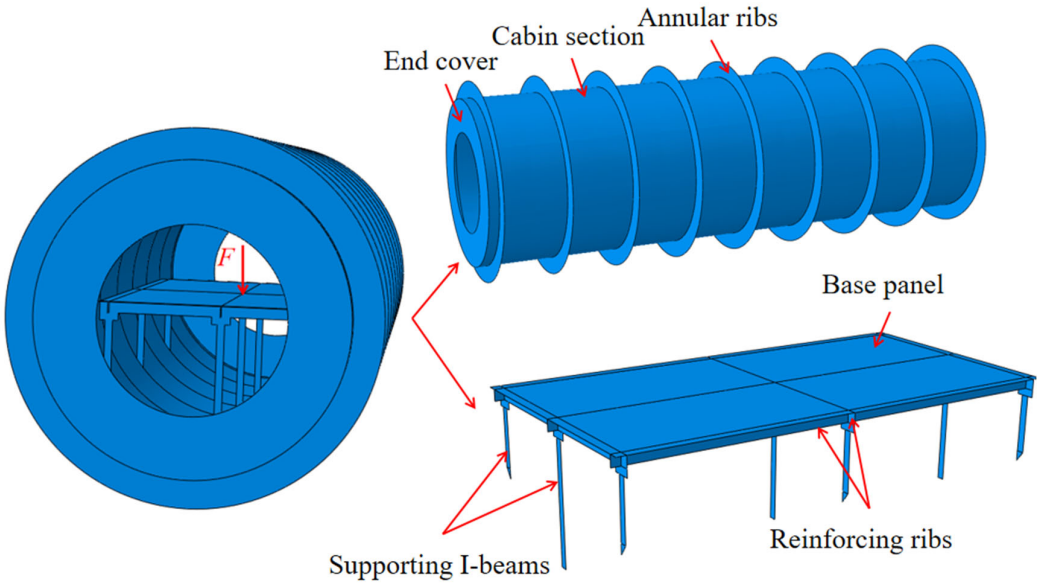


Figure 4. Finite element model of the base panel of the rotating equipment of the power module of the underwater vehicle.

Table 1. Model geometric scale.

Item	Value	Item	Value
Cabin section diameter/mm	1500	Base panel thickness/mm	10
Shell plate thickness/mm	8	End cover thickness/mm	8
Rib height/mm	150	I-beam web height/mm	626
Rib plate thickness/mm	8	I-beam web thickness/mm	40
Base panel length/mm	1300	I-beam panel height/mm	528
Base panel width/mm	2500	I-beam panel thickness/mm	40

The basic material used for the model is steel, and the material parameters are listed in Table 2. To ensure calculation accuracy while balancing efficiency, components such as shell plates, ribs, and I-beams were modeled using shell elements. To simulate the vertical force exerted on the base panel during the operation of rotating equipment, a vertical, single-frequency, unit sinusoidal excitation force F was applied at the area center of the rectangular region on the upper surface of the base panel, as shown in Figure 4. The excitation frequency range was set to 10~300 Hz. The structural vibration response was calculated: for each frequency, the vibration accelerations of all nodes on the base panel were extracted and compared to find the maximum acceleration. Then, a function curve

of the maximum acceleration varying with frequency was plotted, yielding the frequency curve of the maximum vibration acceleration as shown in Figure 5.

Table 2. Material parameters table.

Material	Density/kg.m^{-3}	Elastic Modulus/GPa	Poisson's Ratio	Loss Factor
steel	7850	210	0.3	0.005
damping	980	0.1	0.45	0.9

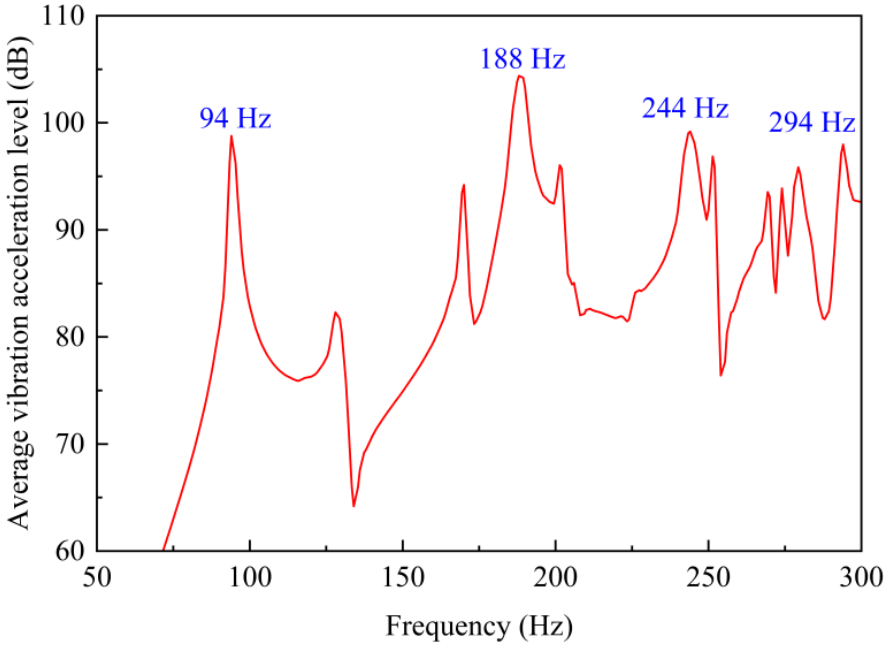
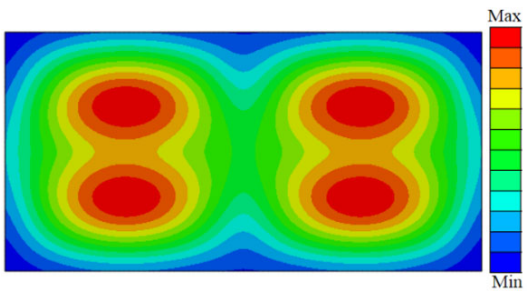
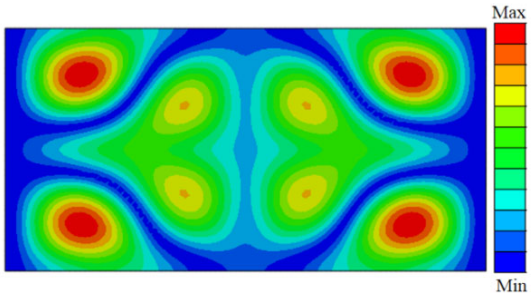


Figure 5. Vibration response of the base panel.

Four distinct vibration peaks can be clearly identified from the figure, corresponding to frequencies of 94 Hz, 188 Hz, 244 Hz, and 294 Hz. These four peak frequencies are denoted as f_1~f_4, respectively, and their corresponding positions of the anti-nodes on the base panel are denoted as P_1~P_4, respectively, as shown in Figure 6. Additionally, P_1 and P_3, P_2 and P_4 are distributed at close distances. This analysis result provides clear target frequencies and application positions for the subsequent design and installation of the GVTC damping plate.

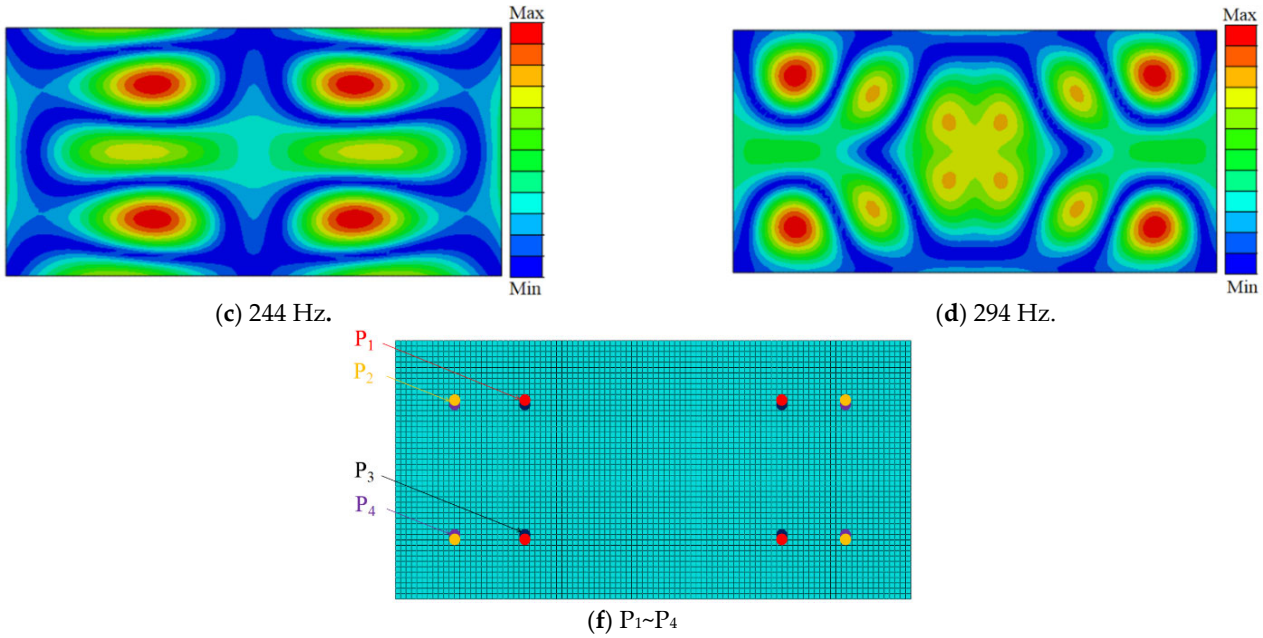


(**a**) 94 Hz.



(**b**) 188 Hz.

Figure 6. *Cont.*



(**c**) 244 Hz. (**d**) 294 Hz.

(**f**) P1~P4

Figure 6. Position map.

3.2. Design of the GVTC Damping Plate

3.2.1. Mesh Generation Method

As an external vibration control device, the GVTC damping plate can be fixed to the vibration peak positions of the base panel in the form of a single plate or a combination of multiple plates to realize efficient absorption of vibration energy. A multi-level GVTC damping plate (as shown in Figure 7) is formed by combining two single damping plates to tackle the multi-order resonance issue of the base panel.

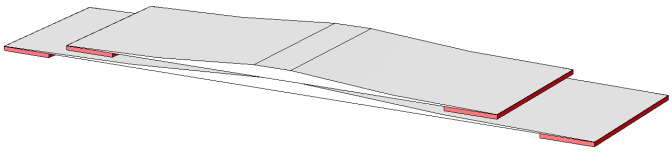
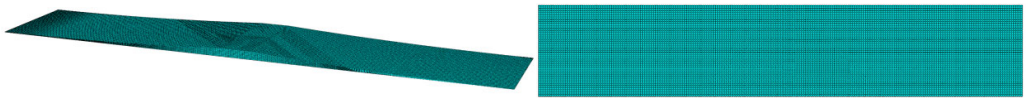


Figure 7. Multi-level GVTC damping plate.

The accuracy of mesh generation directly influences the simulation accuracy of structural wave concentration effects in numerical simulations. Generally, it is required to divide no less than 10 meshes within each structural wavelength range. For the GVTC damping plate in this study, with parameters of a minimum thickness of 0.2 mm and a maximum excitation frequency of 300 Hz, the wavelength at the minimum thickness position was calculated as 76 mm using the wavelength Equation (8), and the mesh size was determined to be 7 mm accordingly. Three-dimensional solid elements and two-dimensional shell elements were used to divide the mesh of the damping plate, respectively, and field functions were used to assign values to the gradient variable-thickness region to simulate its geometric characteristics. The mesh generation results of the two modeling methods are shown in Figure 8. The first three orders of natural frequencies of the two models were calculated and compared (as shown in Table 3), and the results showed that the relative discrepancies were all less than 0.6%, satisfying the accuracy requirements. In terms of the number of elements, the solid element model contains 61,276 nodes and 53,200 elements, while the shell element model only contains 6808 nodes and 6650 elements. The number of solid elements is approximately 10 times that of shell elements. Considering both calcula-

tion accuracy and efficiency, shell elements were finally selected for subsequent modeling and analysis.

$$\lambda = \frac{c_b}{f} = \sqrt{\frac{2\pi h(x)}{f}} \left[\frac{E}{12\rho(1-\mu^2)} \right]^{\frac{1}{4}} \tag{8}$$



(**a**) Solid element. (**b**) Shell element.

Figure 8. Mesh division schematic of modeling with different elements.

Table 3. Calculation results of natural characteristics of GVTC damping plate.

Order	Natural Characteristics	Solid Element Modeling	Shell Element Modeling	Relative Discrepance
First-order mode	Vibration mode			0.5%
	Frequency/Hz	105.1	104.5	
Second-order mode	Vibration mode			0.34%
	Frequency/Hz	117.7	118.1	
Third-order mode	Vibration mode			0.31%
	Frequency/Hz	228.4	229.1	

3.2.2. Parametric Analysis of GVTC Damping Plate

The GVTC damping plate is illustrated in Figure 9, with an overall length of 530 mm. The uniform-thickness region has a thickness of 8 mm, and the minimum thickness of the structure is 0.2 mm; the length of the single-sided gradient variable-thickness region is 250 mm, with a power exponent of 2, and the thickness variation in this region satisfies the power-law function relationship expressed in Equation (9); the material is steel. In this section, the average acceleration level of all nodes in the uniform-thickness region is used as the evaluation index to explore the variation law of its parameters.

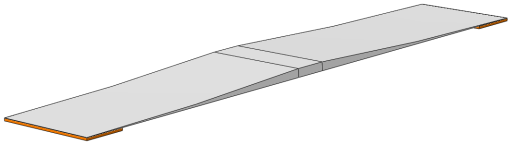


Figure 9. GVTC damping plate.

The boundary condition is set to free, with the excitation point located at the center of the uniform-thickness region. The excitation load is a unit force (direction: perpendicular to the plate surface), and the calculation frequency range is 2~600 Hz with a step size of 2 Hz.

$$h(x) = 7.8 \times \left(\frac{x}{250} \right)^2 + 0.2 \tag{9}$$

(1) Minimum thickness h_1

While keeping the geometric parameters and other material characteristic parameters of the GVTC damping plate unchanged, four groups of working conditions with minimum thicknesses of 0.1 mm, 0.2 mm, 0.3 mm, and 0.4 mm were selected for comparative

analysis. Figure 10 presents the vibration response curves of the plate under different minimum thicknesses.

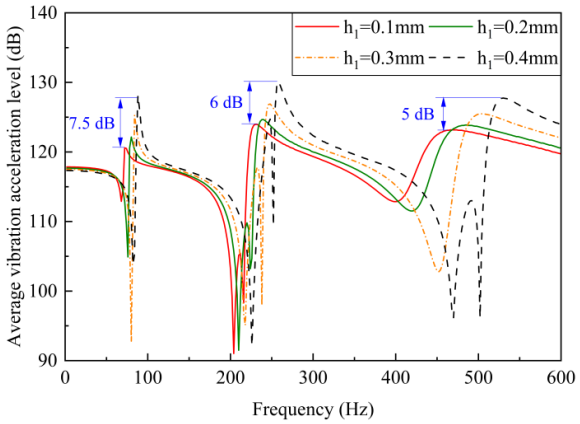


Figure 10. Vibration responses of GVTC damping plates under different minimum thicknesses.

As can be seen from Figure 10, within the frequency range of 2~600 Hz, as the minimum thickness of the GVTC damping plate increases from 0.1 mm to 0.4 mm, the vibration response peak exhibits a significant upward trend. Specifically, the vibration peak of the damping plate with a minimum thickness of 0.1 mm is reduced by 7.5 dB compared with that of 0.4 mm. Meanwhile, the peak of the vibration response curve shifts to the low-frequency band as the minimum thickness decreases, indicating that a smaller minimum thickness improves the structure's ability to suppress low-frequency vibrations. Therefore, on the premise that the processing technology allows, to obtain a better vibration reduction effect, priority should be given to selecting GVTC damping plates with a smaller minimum thickness.

(2) Damping layer loss factor η

Similarly, four groups of working conditions with damping layer loss factors of 0.3, 0.5, 0.7, and 0.9 were selected for comparative analysis, and the vibration response curves of the GVTC damping plate are shown in Figure 11.

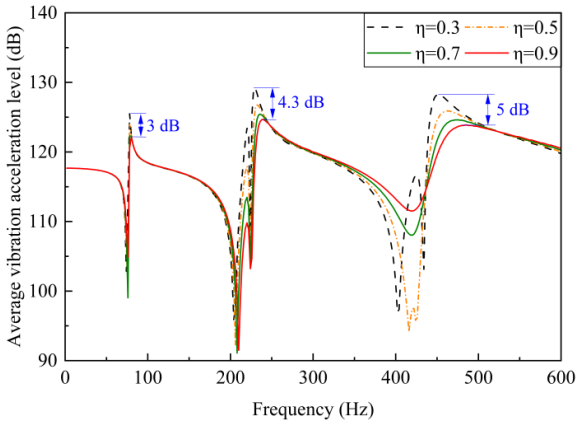


Figure 11. Vibration responses of GVTC damping plates under different damping layer loss factors.

As can be seen from Figure 11 within the frequency range of 2~600 Hz, as the loss factor increases from 0.3 to 0.9, the vibration response peak of the GVTC damping plate exhibits a downward trend. The vibration peak of the damping plate with a loss factor of 0.9 is reduced by 5 dB compared with that with a loss factor of 0.3, indicating that the larger the loss factor, the more significant the vibration suppression effect. Therefore, to obtain a

better vibration reduction effect, priority should be given to selecting damping materials with a larger loss factor.

3.2.3. Design of Composite Damping Plate

In the setting of boundary conditions, the upper surface of the uniform thickness region of the GVTC damping plate was set as a fixed constraint, and the other two ends were kept free. By adjusting the length of the gradient variable-thickness region, the first-order natural frequencies of B_1~B_4 were matched with f_1~f_4, respectively (the specific frequency values are shown in Table 4). Taking B_1 as an example, as indicated in Section 3.2.2, a smaller minimum thickness h1 leads to better vibration control performance; thus, h1 is set to 0.2 mm. Figure 12 shows the correlation between the length of its gradient variable-thickness region and the first-order natural frequency. Considering the close-distance distribution characteristics of P_1 and P_3, P_2 and P_4 on the base panel, B_1 and B_3 were stacked to form a multi-level GVTC damping plate B_{13}, and B_2 and B_4 were stacked to form a multi-level GVTC damping plate B_{24}. The natural characteristics of the two multi-level damping plates are shown in Table 5. Figure 13 shows the modal diagram of peak superposition between the GVTC damping plate and the base panel.

Table 4. First-order natural frequency of GVTC damping plate.

GVTC Damping Plate	B_1	B_2	B_3	B_4
First-order natural frequency/Hz	93.4	187	243.1	293.2

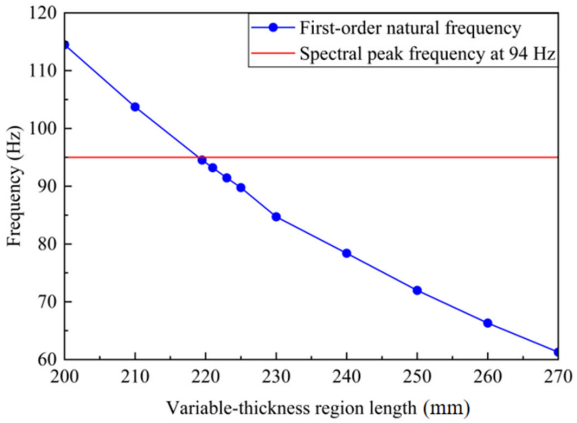
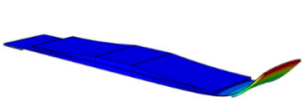
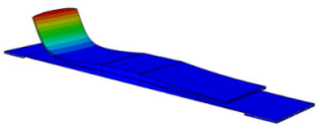
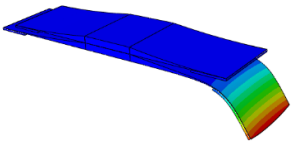
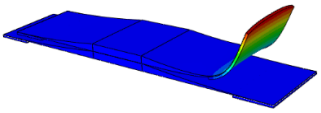
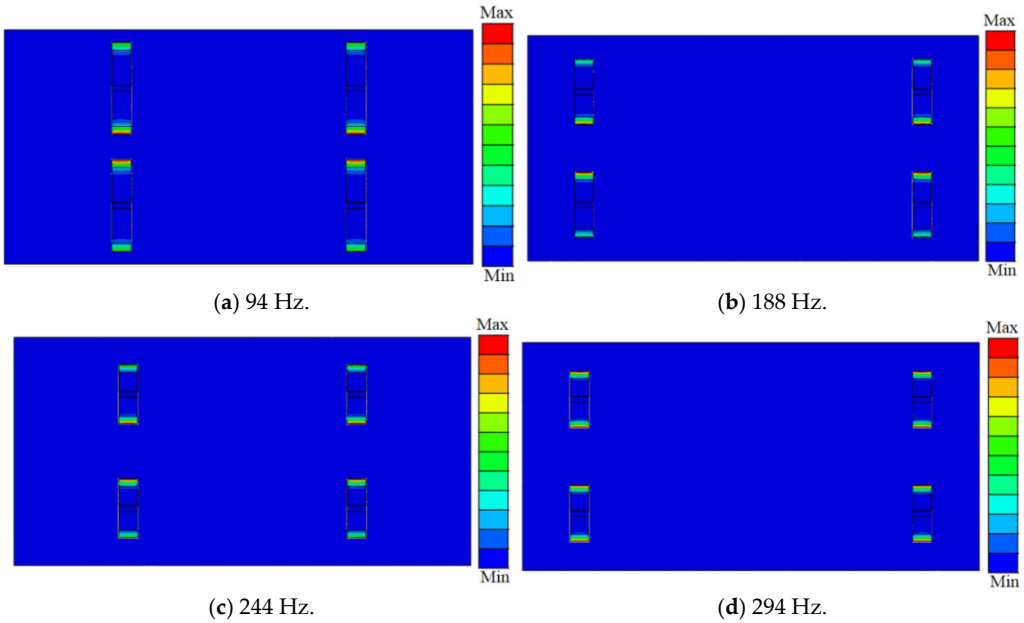


Figure 12. Variation in first-order natural frequency of GVTC damping plate with length of its thickness-variable region (taking B_1 as an example).

Table 5. Natural characteristics of multi-level GVTC damping plate.

Multi-Level GVTC Damping Plate	Natural Characteristics	First-Order Mode	Fifth-Order Mode
B_{13}	Vibration mode		
	Frequency/Hz	93.4	243.1
B_{24}	Vibration mode		
	Frequency/Hz	187	293.2



(**a**) 94 Hz. (**b**) 188 Hz.

(**c**) 244 Hz. (**d**) 294 Hz.

Figure 13. Modal diagram of peak superposition between the GVTC damping plate and the base panel.

The main structural parameters of the damping plates are as follows: the width is 100 mm for all, the thickness of the uniform-thickness region is 8 mm, the power exponent of the gradient variable-thickness region is 2, and the lengths of the gradient variable-thickness regions of B_1~B_4 are 224 mm, 141 mm, 160 mm, and 127 mm, respectively. The main material used is steel (material parameters are shown in Table 2) to ensure that its mechanical properties are compatible with the base structure.

3.2.4. Vibration Analysis of the Base Panel with the GVTC Damping Plate Installed

To validate the vibration control effect of the GVTC damping plate, the designed B_{13} and B_{24} damping plates were fixed at the corresponding positions below the base panel (as shown in Figure 14), and an equivalent mass block model was established (as shown in Figure 15) to exclude the interference of pure mass addition on the vibration reduction effect. Calculations were performed within the frequency range of 10~300 Hz to obtain the average vibration acceleration level A_s of the base panel before and after installing the damping plate, and when the equivalent mass block was installed (as shown in Figure 16). The specific data comparison is shown in Table 6. The calculation formula is:

$$A_s = 20\lg\left[\frac{1}{n}\sum_{1}^{n}\frac{a_i}{a_0}\right] \tag{10}$$

where a_i is the acceleration value of the i-th node, $i = 1, 2, 3, \cdots, n$, and n is the total number of nodes in the model, a_0 is the reference acceleration, with a value of 0.001 mm/s^2.

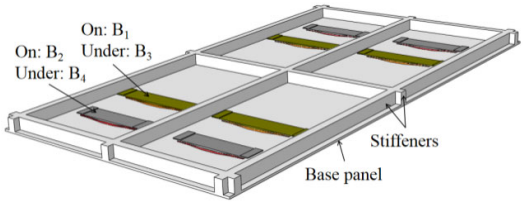


Figure 14. Installation schematic of GVTC damping plate.

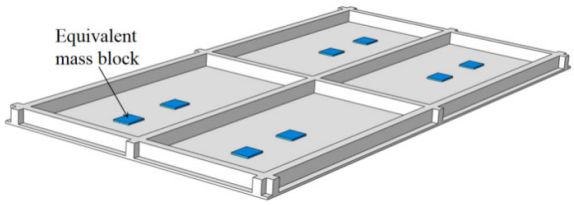


Figure 15. Installation schematic of equivalent mass block model.

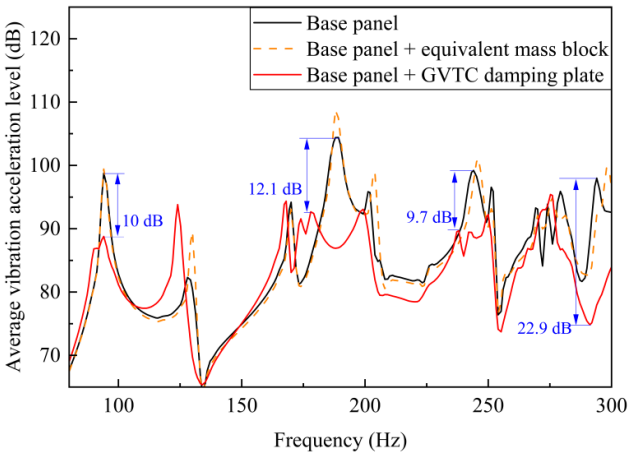


Figure 16. Vibration responses of the base panel under the equivalent mass block: before and after installing the GVTC damping plate.

Table 6. Comparison of vibration responses of the base panel.

Peak Frequency/Hz	Before Installation-Average Vibration Acceleration Level/dB	After Installation-Average Vibration Acceleration Level/dB	Equivalent Mass Block-Average Vibration Acceleration Level/dB
94	98.8	88.8	99.4
188	104.4	92.3	108.7
244	99.2	89.5	101.1
294	98	75.1	99.7

The analysis results show that, within the target frequency range, the GVTC damping plate exhibits a significant suppression effect on the vibration peaks of the base panel: the vibration peak at 94 Hz is reduced by 10 dB, at 188 Hz by 12.1 dB, at 244 Hz by 9.7 dB, and at 294 Hz by 22.9 dB, with the most prominent vibration reduction effect. Meanwhile, the additional mass of the damping plate only constitutes 1.53% of the mass of the base panel, meeting the lightweight requirement. However, after installing the equivalent mass block, the vibration peaks of the base panel did not show significant reduction and even increased slightly at certain frequencies. This further verifies that the vibration reduction effect of the damping plate stems from the synergistic effect of its ABH effect and anti-resonance effect, rather than pure mass addition.

The GVTC damping plate is fixedly connected to the base panel via its own uniform-thickness region (8 mm thick, steel material), which acts as a local stiffener for the base panel (10 mm thick) and slightly increases the local stiffness of the base panel at the installation position. Modal reanalysis of the base panel with the damping plate installed reveals that the 125 Hz peak corresponds to the 2nd-order local bending mode of the middle area of the base panel (between P_1 and P_2), which is excited by the stiffness adjustment induced by the fixed end of the damping plate. This mode was not prominent in the original base panel

(without the damping plate) due to its low vibration amplitude, and it is amplified under the combined action of excitation and local stiffness variation, thus forming a visible peak.

3.2.5. Expandability of the GVTC Damping Plate

GVTC damping plates can be categorized as linear, curved and spiral types according to their structural shapes. Among them, the structural form of the curved GVTC damping plate is shown in Figure 17, and the thickness expression of its variable-thickness region is given as follows:

$$h(\theta) = \begin{cases} h_0 (0 \le \theta \le \theta_1) \\ (h_0 - h_1)\left(\frac{\Theta - \theta + \theta_1}{\Theta}\right)^m + h_1 (\theta_1 \le \theta \le \theta_2) \end{cases} \quad (11)$$

where Θ denotes the angular span of the variable-thickness region, with $\Theta = \theta_2 - \theta_1$; θ_d represents the angular span of the damping layer.

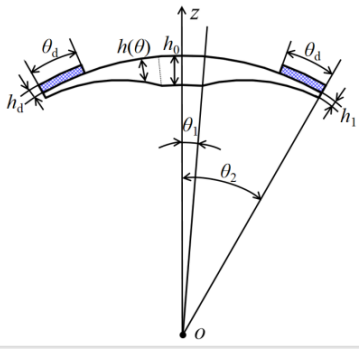


Figure 17. GVTC damping plate.

The design method of the curved GVTC damping plate is consistent with that in Section 3.2.2. This section only presents the cylindrical shell structure with the curved GVTC damping plate attached, as well as the comparative results of its vibration responses before and after installation. The cylindrical shell with CVTC damping plates installed is shown in Figure 18, and the vibration response results are presented in Figure 19.

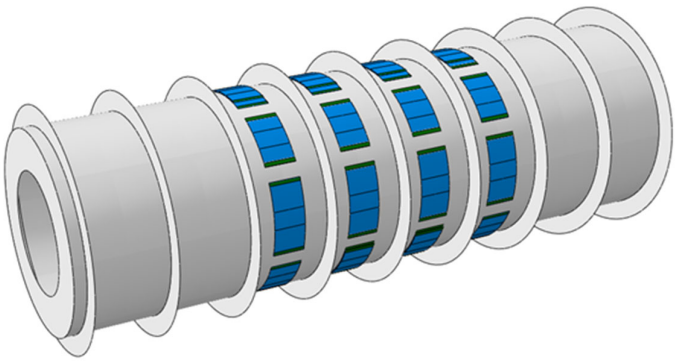


Figure 18. Installation schematic of GVTC damping plate.

The analysis results indicate that, within the target frequency band, the GVTC damping plate significantly suppresses the vibration peaks of the cylindrical shell: the vibration peak at 390 Hz is reduced by 9 dB, the peak at 470 Hz by 11.7 dB, and the peak at 526 Hz by 21.7 dB (the most prominent vibration reduction effect). This further confirms the vibration attenuation performance of the damping plate.

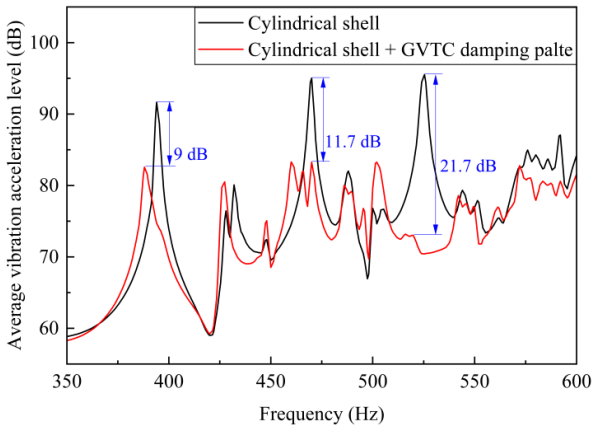


Figure 19. Vibration response of the cylindrical shell before and after installing the GVTC damping plate.

4. Experimental Validation

To validate the actual vibration reduction effect of the GVTC damping plate on the base panel and the reliability of the finite element analysis results, this chapter designs and conducts vibration characteristic tests. By building a test platform, setting up multiple groups of comparative working conditions, and collecting and analyzing test data, the engineering application performance of the composite damping plate was systematically evaluated.

4.1. Construction of the Test Platform

4.1.1. Preparation of Test Model

The main body of the test model (cylindrical shell-base structure) was processed using Q235B carbon steel to ensure consistency with the base material used in practical engineering applications, and the physical appearance of the base is shown in Figure 20. To accommodate different excitation positions and vibration reduction requirements, 8 types of GVTC damping plates (denoted as B_1~B_8) were designed and manufactured. Among them, B_1~B_4 are consistent with the composite damping plates designed in Section 3.2.3, and the core difference lies in the power function parameters of the gradient variable-thickness region, which are customized to align with the resonance characteristics of the base panel in different frequency bands.

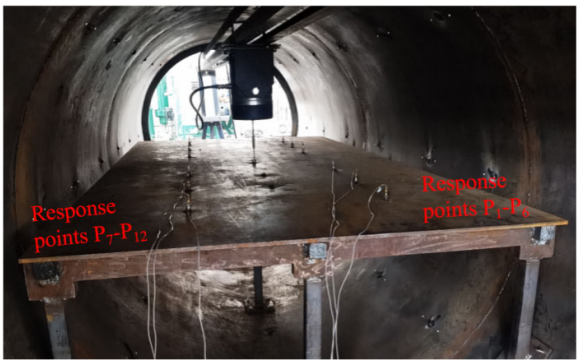


Figure 20. Physical image of the base panel.

4.1.2. Design of Test Working Conditions

To exclude interference factors such as excitation position, four groups of comparative working conditions were set up, and the specific schemes are as follows:

(1) Working condition 1 (Benchmark condition): Only the base panel was retained, and excitation was applied at the center of the panel to obtain the vibration response of the base without any vibration reduction measures.

(2) Working condition 2 (Central excitation + damping plates): On the basis of working condition 1, 16 composite damping plates (4 pieces each of B_1, B_2, B_3, and B_4) were fastened to the back of the base panel using bolts and nuts. The installation positions referred to Figure 14, and the excitation point remained unchanged (at the center of the panel). A partial view of the installation site is shown in Figure 21.

(3) Working condition 3 (Offset excitation benchmark): Only the base panel was retained, and the excitation point was adjusted to 600 mm away from the center of the panel to simulate the scenario of excitation position offset in practical applications and obtain the vibration response under this scenario.

(4) Working condition 4 (Offset excitation + damping plates): On the basis of working condition 3, 8 composite damping plates (2 pieces each of B_5, B_6, B_7, and B_8) were fixed on the back of the base panel. The main structural parameters of the damping plates are as follows: the width is 100 mm for all, the thickness of the uniform thickness region is 10 mm, the power exponent is 2, and the lengths of the gradient variable-thickness regions of B_5~B_8 are 200.5 mm, 245 mm, 164.5 mm, and 143.5 mm, respectively. The installation positions referred to Figure 22, and the excitation point remained consistent with that in working condition 3. A partial view of the installation site is shown in Figure 23.



Figure 21. On-site image of partial area under working condition 2.

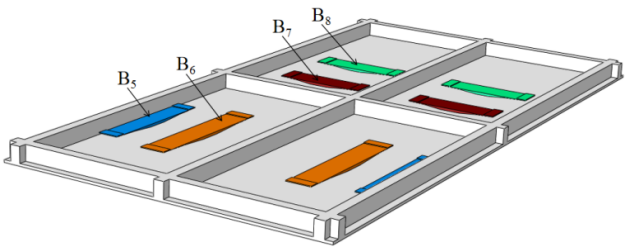


Figure 22. Installation schematic of GVTC damping plate.



Figure 23. On-site image of partial area under working condition 4.

4.1.3. Composition of the Test System

The test system comprises two parts: the excitation system and the measurement system, and the overall structure is shown in Figure 24:

(1) Excitation system: Composed of a signal generator, a HEA-500G power amplifier, and a HEA-500 exciter (both from Nanjing Foneng Technology Industry Co., Ltd., Nanjing, China), it can output sinusoidal excitation signals with a frequency range of 10~300 Hz. The excitation force is collected in real time by a force sensor installed between the excitation rod and the base panel.

(2) Measurement system: Includes a B&K 2635 charge amplifier, B&K 4508B acceleration sensors, B&K 208C03 force sensor (all from Brüel & Kjær Sound & Vibration Measurement A/S, Nærum, Denmark), a 32-channel LMS signal acquisition instrument (from Siemens Industry Software Inc., Leuven, Belgium), and a computer. Twelve vibration response evaluation points (P_1~P_{12}) were selected on the base panel, and the vibration acceleration signals at each point were collected by the acceleration sensors. Finally, the average vibration acceleration level of the 12 evaluation points was used to quantify the overall vibration response of the structure, so as to reduce the impact of boundary effects on the data.

(3) Simulation of boundary conditions: The test model was fixed by flexible suspension to simulate the free boundary conditions in practical engineering, preventing the interference of the test bench stiffness on vibration transmission.

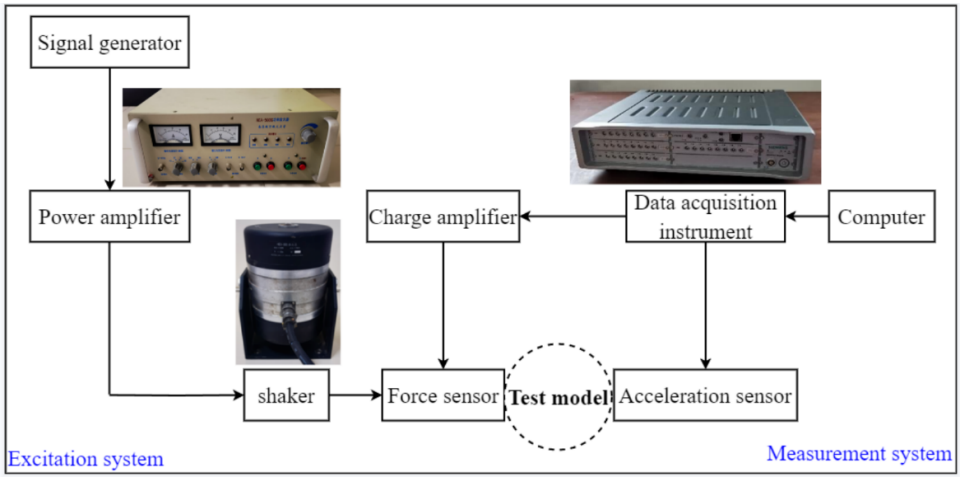


Figure 24. Schematic of vibration transmission characteristics test system.

4.2. Test Results and Analysis

4.2.1. Consistency Verification Between Simulation and Test Results

Taking Working Condition 2 as an example, the amplitude difference in vibration acceleration measured by finite element simulation and the test was compared (as shown in Figure 25, and the results are as follows:

(1) Frequency correspondence: Although there was a slight offset between the resonance peak frequencies identified in the simulation (94 Hz, 188 Hz, 244 Hz) and those identified in the test (82 Hz, 172 Hz, 234 Hz), the overall variation trend was consistent, and the deviation of the average vibration acceleration amplitude difference was small, which confirmed the accuracy of the finite element model.

(2) Analysis of the causes of differences: The frequency offset was mainly caused by slight differences in mass and stiffness between the simulation model and the actual test model; the difference in resonance peak amplitudes was due to the frequency dependence of the material loss factor, making it difficult to accurately match the loss

factor characteristics of the actual material in the simulation. However, this difference did not compromise the judgment of the overall vibration reduction effect.

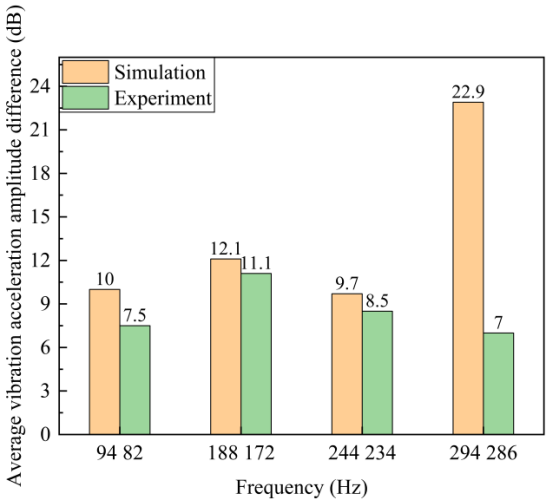


Figure 25. Comparison results of vibration response experiment and simulation.

4.2.2. Evaluation of Vibration Reduction Effect of the Composite Damping Plate

By comparing the vibration response curves under different working conditions (as shown in Figure 26), the vibration reduction performance of the composite damping plate was analyzed:

(1) Comparison between working condition 1 and working condition 2 (Figure 26a): Within the frequency range of 10~300 Hz, after installing the composite damping plates, the vibration response of the base panel was significantly reduced, the number of resonance peaks decreased, and the peak amplitude dropped. Among them, the vibration peaks at 82 Hz, 172 Hz, 244 Hz, and 286 Hz were reduced by 7.5 dB, 11.1 dB, 8.5 dB, and 7 dB, respectively, demonstrating a stable vibration reduction effect.

(2) Comparison between working condition 3 and working condition 4 (Figure 26b): Under the offset excitation scenario, the composite damping plates still demonstrated excellent vibration reduction performance, with a maximum vibration amplitude attenuation of 13.8 dB, and effectively suppressed the new resonance peaks caused by the offset of the excitation position, confirming that it has a certain adaptability to changes in the excitation position.

(3) Core conclusion: Under both excitation scenarios, the composite damping plates can significantly mitigate the low-frequency resonance of the base panel through the energy accumulation of the ABH effect and the vibration cancelation of the anti-resonance effect. Moreover, the proportion of additional mass is low (only 1.53%), which does not place an extra load on the base structure and satisfies the lightweight requirements of engineering applications.

4.3. Analysis of Experimental Uncertainties and Limitations

4.3.1. Analysis of Experimental Measurement Uncertainties

The uncertainties of the experimental measurement results mainly stem from the measurement system error, environmental interference and human operation deviation, as detailed as follows:

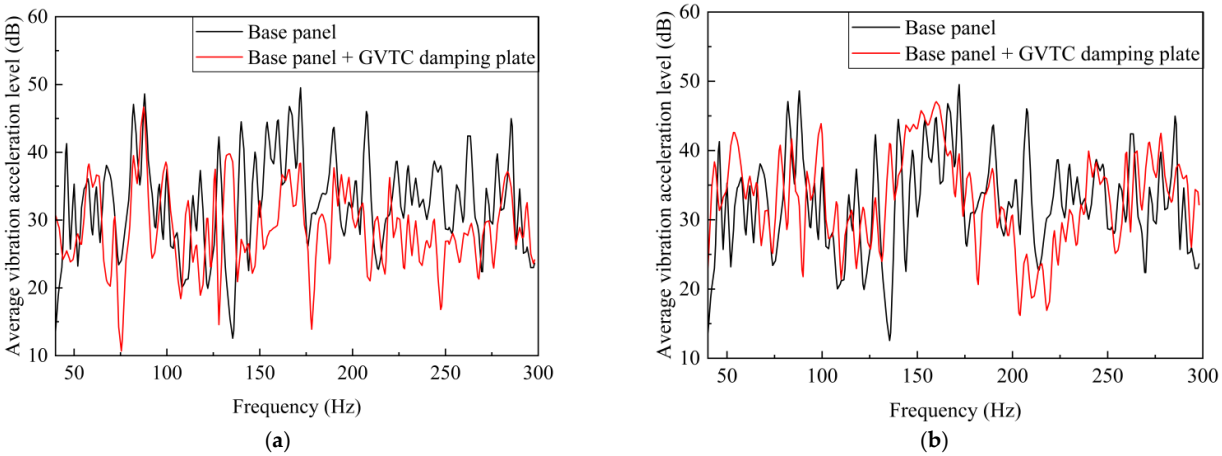


Figure 26. Comparison results of vibration responses under different working conditions: (**a**) Comparison between working condition 1 and working condition 2. (**b**) Comparison between working condition 3 and working condition 4.

(1) Intrinsic error of the measurement system

Sensor accuracy limitation: The adopted acceleration sensor (accuracy class: ±0.5%) and force sensor (accuracy class: ±0.3%) have intrinsic measurement errors. At low frequencies (<50 Hz) with small signal amplitudes, the relative error is amplified to ±1.2~±1.5%, leading to a deviation of ±0.3~0.5 dB in the measurement of resonance peak amplitude.

Signal acquisition and processing error: The sampling frequency of the 32-channel LMS signal acquisition instrument is set to 2048 Hz, which satisfies the Nyquist sampling theorem. However, near the resonance peak frequencies (e.g., 94 Hz, 188 Hz), the limited frequency resolution (0.5 Hz) leads to a deviation of ±1~2 Hz in resonance peak frequency identification, which is partially responsible for the frequency offset between the experimental and simulation results.

Excitation system stability error: The output signal stability of the HEA-500G power amplifier is affected by grid voltage fluctuations (fluctuation range: ±5%), causing a ±3~±5% variation in the excitation force amplitude and thus compromising the consistency of vibration response measurements.

(2) Interference from environmental and boundary conditions

Environmental noise and vibration interference: Ambient noise (45~55 dB) and ground micro-vibrations (acceleration amplitude < 0.001 m/s^2) exist in the test environment. Although flexible suspension (suspension rope stiffness < 0.1 N/m) was adopted to isolate most external vibrations, a slight interference is still imposed on the vibration response measurement in the low-frequency range (10~50 Hz), resulting in an increase of ±0.2~0.4 dB in the measurement deviation of the average vibration acceleration level within this frequency range.

Deviation in boundary condition simulation: A flexible suspension was used to simulate the free boundary in the test. However, the suspension rope has a small damping ratio (<0.01), and there is local stiffness concentration at the connection points with the model. This differs from the ideal free boundary (without damping and additional stiffness) in the simulation, resulting in the measured natural frequency of the structure being lower than the simulated value (e.g., the simulated peak at 94 Hz corresponds to the test peak at 82 Hz).

(3) Human operation deviation

Sensor installation deviation: Twelve acceleration sensors were fixed by welding threaded bases, and an angular deviation of ±0.5~±1° existed during the installation process, resulting in a measurement error of ±2~±3% in the normal acceleration.

Excitation point positioning deviation: The positioning of excitation points for central and offset excitation was measured with a tape measure (accuracy: ±1 mm). A slight deviation from the ideal excitation points in the simulation occurred, which induced changes in the local vibration modes and thus led to amplitude deviations of partial resonance peaks.

4.3.2. Analysis of Experimental Limitations

(1) Discrepancies between the experimental and simulation models

Deviation in material parameter consistency: The elastic modulus (210 GPa) and Poisson's ratio (0.3) of steel adopted in the simulation are theoretical values, while the actually processed Q235B carbon steel has a practical elastic modulus ranging from 205 to 215 GPa and a Poisson's ratio of 0.29 to 0.31 due to smelting process differences, resulting in a ±2–±3% deviation in structural stiffness. The loss factor of the damping material (simulation value: 0.9) is affected by temperature (test ambient temperature: 25 ± 2 °C), with the practical loss factor ranging from 0.85 to 0.95, which impairs the quantitative consistency of energy dissipation performance.

Deviation in structural geometric dimensions: The gradient variable-thickness region of the damping plate is processed by wire cutting. The practical machining error of the minimum thickness (design value: 0.2 mm) is ±0.05 mm, and that of the length of the gradient variable-thickness region (design values: 224 mm, 141 mm, etc.) is ±1 mm. This leads to a ±0.5–1 Hz deviation in the natural frequency of a single damping plate, which compromises the anti-resonance matching accuracy.

(2) Limitations due to the simplification of experimental working conditions

Simplification of excitation form: A single-frequency sinusoidal excitation is adopted in the experiment, whereas the excitation inside the power cabin of an actual underwater vehicle is a complex multi-frequency superposition excitation (including the fundamental and harmonic frequencies of rotating equipment). This discrepancy from the single-frequency excitation boundary condition in the simulation prevents full simulation of the vibration reduction performance under actual working conditions.

Simplification of structural integrity: The experimental model only consists of the base panel and composite damping plate, excluding the integral structure of the power cabin (e.g., the coupling effect of cabin sections, ribs and the base). Although the influence of cabin sections is simulated by the finite element model in the simulation, the coupling stiffness and mass distribution of the actual structure are more complex, resulting in discrepancies in the vibration transmission paths.

5. Conclusions

This study proposed a vibration control scheme utilizing a GVTC damping plate, based on the integrated principles of the ABH effect and anti-resonance theory, to address multi-order resonance in base structures within the 10–300 Hz low-frequency range. Through theoretical modeling, numerical simulation, and experimental verification, the vibration reduction mechanism and engineering performance of the plate are elucidated, and the main conclusions are as follows:

(1) The GVTC damping plate designed in this study emphasizes engineering integration to overcome the application limitations of existing ABH-based vibration control technologies. Compared with traditional base vibration reduction methods (structural

stiffness optimization, rubber vibration isolators, etc.) and existing ABH structures, this composite damping plate achieves three key improvements: no modification to the original base structure, multi-order resonance suppression in the low-frequency band, and lightweight design, which better meets the vibration control needs of finalized equipment. It demonstrates superior vibration reduction performance in the 10~300 Hz low-frequency range, and its additional mass constitutes only 1.53% of the base panel, meeting lightweight requirements. This provides a more flexible technical option for vibration control of finalized equipment.

(2) The shell element modeling method significantly enhances the efficiency of numerical simulation. Compared with solid element modeling, under the premise of ensuring the relative discrepance of the first three-order natural frequencies is <0.6% and maintaining calculation accuracy, the number of elements in the shell element model is approximately 1/10 of that in the solid element model. This greatly lowers the calculation load and provides an efficient simulation tool for parameter optimization and engineering design of the GVTC damping plate.

(3) Finite element analysis and experimental results validate the effectiveness of the composite damping plate in vibration reduction. Within the target frequency range, the damping plate significantly suppresses the vibration peaks of the base panel at 94 Hz, 188 Hz, 244 Hz, and 294 Hz, with a maximum vibration reduction of 22.9 dB. In the experiment, the maximum attenuation of vibration amplitude reaches 13.8 dB, and the resonance peak frequencies and the variation trends of acceleration amplitude in simulation and experiment are in good agreement, confirming the reliability and accuracy of the design scheme.

(4) The GVTC damping plate paves the way for the engineering application of ABH technology. With the external installation design, the damping plate achieves precise suppression of multi-order resonance peaks without weakening the strength of the base itself, addressing the problems of high processing difficulty and narrow vibration control frequency range of traditional ABH structures.

Author Contributions: Conceptualization, W.L. and Q.Y.; Methodology, W.L., Y.Z. and Q.Y.; Validation, Y.Z., L.T., M.T. and J.D.; Writing—original draft, Y.Z. and M.T.; Writing—review & editing, L.T., J.D., J.L. and Q.Y.; Project administration, J.H.; Funding acquisition, J.H. All authors have read and agreed to the published version of the manuscript.

Funding: Supported by the National Natural Science Foundation of China (No. 52071334).

Data Availability Statement: The original contributions presented in this study are included in the article. Further inquiries can be directed to the corresponding author(s).

Conflicts of Interest: The author declares no conflicts of interest.

References

1. Du, M.B.; Yang, Y.; Yuan, Y.C.; Tang, W.Y. Vibration analysis and control technology of marine main engine base system. *Ship Eng.* **2024**, *46*, 14–30.
2. Wu, Y.; Dai, Q.; Liu, H.; Tang, Y.; Chen, X.C. Ship base vibration reduction design technology based on visualization of power flow and discrete optimization. *Ocean Eng.* **2024**, *309*, 118494. [CrossRef]
3. Zhu, Q.Y.; Han, Q.K.; Wang, W.M.; Jiang, Z.N. Vibration transmission path analysis of multi-support accessory system for aero-engine. *Acta Aeronaut. Astronaut. Sin.* **2024**, *45*, 57–72.
4. Wei, J.H.; Xiang, Y. Research on improving acoustic stealth performance of unmanned underwater vehicles. *Noise Vib. Control* **2024**, *44*, 206–211+272.
5. Zhang, X.; Li, J.B.; Chen, L.; Li, J.T.; Ye, F.; Ye, X. Optimization design and experimental research on vibration reduction of marine power equipment base. *Noise Vib. Control* **2023**, *43*, 196–201.

6. Qiu, P.; Li, G.C. Research progress and trend of vibration and noise prediction in ship cabins. *China Water Transp.* **2023**, *15*, 72–73. [CrossRef]
7. Wang, Y.Y.; Yang, D.Q. Acoustic design of base with synchronous optimization of vibration-Isolating mass-stiffness-damping material configuration. *J. Vib. Shock* **2021**, *40*, 257–264.
8. Wang, J.W. Scheme design and vibration isolation performance research of a new marine vibration isolator. *Ship Electron. Eng.* **2022**, *42*, 164–168.
9. Zhu, C.Y.; Wen, H.B. Experimental research on vibration reduction of base by butyl rubber damping material. *Shipbuild. Technol.* **2015**, 50–53.
10. Du, Y.H.; Hu, S.Q.; Du, Q. Research on calculation method for nonlinear dynamic characteristics of rubber vibration isolators. *Struct. Environ. Eng.* **2022**, *49*, 36–44.
11. Li, Y.; Huang, X.C.; Su, Z.W.; Jiao, S.J.; Zheng, Z.W.; Zhang, X.R. Simulation and experiment of a rubber vibration isolator with small dynamic-static stiffness ratio. *Noise Vib. Control* **2024**, *44*, 256–260.
12. Zhou, X.; Wu, K.; Zou, X.J. Research on vibration reduction characteristics of high-damping alloy base. *Ship Eng.* **2024**, *46*, 90–95+104.
13. Xia, Z.W.; Shi, D.X.; Yang, Q.; Cao, R.; Wan, Y.; Liu, Y.S. Vibration reduction performance analysis of marine base structure based on vibration-isolating mass. *Noise Vib. Control* **2023**, *43*, 227–231.
14. Mironov, M.A. Propagation of a flexural wave in a plate whose thickness decreases smoothly to zero in a finite interval. *Sov. Phys. -Acoust.* **1988**, *34*, 318–319.
15. Pekeris, L.C. Theory of propagation of sound in a half-space of variable sound velocity under conditions of formation of a shadow zone. *J. Acoust. Soc. Am.* **1946**, *18*, 295–315. [CrossRef]
16. Luo, X.; Wang, X.; Fan, Q.; Wang, J.; Shi, Y.Y.; Liu, J.Q.; Huang, Y.Z. Research on vibration reduction characteristics and optimization of an embedded symmetric distribution multi-level acoustic black hole floating raft isolation system. *Symmetry* **2025**, *17*, 1196. [CrossRef]
17. Guasch, O.; Patricia Sánchez-Martín Ghilardi, D. Application of the transfer matrix approximation for wave propagation in a metafluid representing an acoustic black hole duct termination. *Appl. Math. Model.* **2020**, *77*, 1881–1893. [CrossRef]
18. Krylov, V.V.; Shuvalov, A.L. Propagation of localised flexural vibrations along plate edges described by a power law. *Inst. Acoust.* **2000**, *22*, 263–270.
19. Krylov, V.V. Localized acoustic modes of a quadratically-shaped solid wedge. *Mosc. Univ. Phys. Bull.* **1990**, *45*, 65–69.
20. Conlon, S.C.; Fahnline, J.B.; Semperlotti, F. Numerical analysis of the vibroacoustic properties of plates with embedded grids of acoustic black holes. *J. Acoust. Soc. Am.* **2015**, *137*, 447. [CrossRef] [PubMed]
21. Zhao, L. Low-frequency vibration reduction using a sandwich plate with periodically embedded acoustic black holes. *J. Sound Vib.* **2019**, *441*, 165–171. [CrossRef]
22. He, P.; Wang, X.D.; Ji, H.L.; Qiu, J.H.; Cheng, L. Full-frequency band vibration control of box structure based on acoustic black hole. *Acta Aeronaut. Astronaut. Sin.* **2020**, *41*, 134–143.
23. Zhao, Y.N.; Yang, D.Q.; Wang, B.H. Application research of acoustic black hole energy harvester in noise control of air-cushion ship cabins. *Shipbuild. China* **2020**, *61*, 58–67.
24. Zhao, N.; Wang, Y.; Chen, L.; Pang, F.Z. Research on vibration isolation performance of distributed acoustic black hole floating raft system. *J. Vib. Shock* **2022**, *41*, 75–80.
25. Xia, J.C. *Research on Vibration Reduction Base of Power Equipment Based on Acoustic Black Hole Effect*; Harbin Engineering University: Harbin, China, 2024.
26. Krylov, V.V.; Tilman, F.J.B.S. Acoustic 'black holes' for flexural waves as effective vibration dampers. *J. Sound Vib.* **2004**, *274*, 605–619. [CrossRef]
27. Mironov, A.M.; Pislyakov, V.V. One-Dimensional acoustic waves in retarding structures with propagation velocity tending to zero. *Acoust. Phys.* **2002**, *48*, 347–352. [CrossRef]
28. Conlon, S.C.; Fahnline, J.B.; Semperlotti, F.; Feurtado, P.A. Enhancing the low frequency vibration reduction performance of plates with embedded acoustic black holes. In Proceedings of the InterNoise14, Melbourne, Australia, 16–19 November 2014; pp. 175–182.
29. Krylov, V.V. On the velocities of localized vibration modes in immersed solid wedges. *J. Acoust. Soc. Am.* **1998**, *103*, 767–770. [CrossRef]
30. Ji, H.L.; Huang, W.; Qiu, J.H.; Cheng, L. Mechanical Problems in the Application of Acoustic Black Hole Structures. *Adv. Mech.* **2017**, *47*, 333–384.
31. Krylov, V.V. Conditions for validity of the geometrical-acoustics approximation in application to waves in an acute-angle solid wedge. *Sov. Phys. Acoust.* **1989**, *35*, 176–180.
32. Krylov, V.V. Geometrical-acoustics approach to the description of localized vibrational modes of an elastic solid wedge. *Sov. Phys.-Tech. Phys.* **1990**, *35*, 137–140.

33. Climente, A.; Torrent, D.; Sanchez-Dehesa, J. Gradient index lenses for flexural waves based on thickness variations. *Appl. Phys. Lett.* **2014**, *105*, 115. [CrossRef]
34. Krylov, V.V. New type of vibration dampers utilising the effect of acoustic 'black holes'. *Acta Acust. United Acust.* **2004**, *90*, 830–837.
35. Conlon, S.C.; Semperlotti, F.; Fahnline, J.B. Passive control of vibration and sound transmission for vehicle structures via embedded acoustic black holes. In Proceedings of the InterNoise13, Innsbruck, Austria, 15–18 September 2013; pp. 176–184.
36. Bowyer, E.P.; O'Boy, D.J.; Krylov, V.V. Damping of flexural vibrations in plates containing ensembles of tapered indentations of power-law profile. *J. Acoust. Soc. Am.* **2013**, *132*, 2041.
37. Bowyer, P.E.; Krylov, V.V. Sound radiation of rectangular plates containing tapered indentations of power-law profile. *J. Acoust. Soc. Am.* **2012**, *132*, 2041. [CrossRef]
38. Denis, V.; Gautier, F.; Pelat, A.; Poittevin, J. Measurement and modelling of the reflection coefficient of an Acoustic Black Hole termination. *J. Sound Vib.* **2015**, *349*, 67–79. [CrossRef]

Disclaimer/Publisher's Note: The statements, opinions and data contained in all publications are solely those of the individual author(s) and contributor(s) and not of MDPI and/or the editor(s). MDPI and/or the editor(s) disclaim responsibility for any injury to people or property resulting from any ideas, methods, instructions or products referred to in the content.